

# A Novel Articulating Bone Cutting Tool for Minimally Invasive Craniostosis Surgery

## Jones Law

PhD Candidate  
The CIGITI Lab  
The Hospital for Sick Children  
The Institute of Biomedical Engineering  
University of Toronto  
Email: jones.law@mail.utoronto.ca

## Emma Stickley

Technologist  
The CIGITI Lab  
The Hospital for Sick Children

## Thomas Looi

Assistant Professor  
The CIGITI Lab  
The Hospital for Sick Children  
University of Toronto

## Eric Diller

Associate Professor  
Microrobotics Laboratory  
The Institute of Biomedical Engineering  
University of Toronto

## Dale Podolsky

Associate Professor  
The CIGITI Lab  
The Institute of Biomedical Engineering  
The Hospital for Sick Children

Craniosynostosis involves early fusion of cranial sutures, resulting in an abnormal head shape and functional issues such as elevated intracranial pressure. Treatment involves surgery to correct the head shape and to allow unrestricted brain growth. This work aims to overcome the restrictions of current instruments by developing a novel articulated bone cutting tool for minimally invasive craniostosis surgery. A handheld tendon-driven tool with a bending section was developed to enhance reachability along the skull. The tool comprises a driving unit, a bending section attached to an end-effector, and a flexible endoscope. The prototype was developed and characterized to validate its accuracy, stiffness, bone-cutting capability, and reachability. A prototype was developed with a high reachability of 72.2%, 71.6%, 78.4% (length of the osteotomy/total planned path) using sagittal, metopic and unicoronal cran-

iosynostosis skull models, respectively. The tool demonstrated low deflection ( $\leq 5$  mm for all configurations except for  $0^\circ$  bending) under 5 N external force and is capable of cutting bone-like materials with varying bending angles (range from  $45^\circ$  to  $90^\circ$ ). These results indicate the potential of the bone-cutting tool to provide a paradigm shift in the treatment of craniostosis, expanding the benefits of minimally invasive approach to more patients.

## 1 INTRODUCTION

Craniosynostosis is a condition that involves premature fusion of the cranial sutures, leading to an abnormal head shape and functional consequences such as elevated intracranial pressure, neurocognitive deficits, and

psychosocial issues [1][2][3]. The condition occurs in approximately 3.5 to 4.5 out of 10,000 births worldwide [4]. Treatment involves surgical intervention to correct the head shape and to allow for unrestricted brain growth. Typically, this procedure is performed on infants who are 2-12 months of age or older. Surgery can be performed either open or endoscopically, with both approaches requiring osteotomies (bone cuts) to remodel the cranium.

During open surgery, a large bicoronal incision is required to access the cranium and perform extensive osteotomies and bony reshaping. This approach provides maximum exposure and control, but is invasive with significant blood loss, long operating time [5], and prolonged recovery time in hospital [6]. There is an evolution toward minimally invasive endoscopic approaches that require smaller incisions with less blood loss and shorter procedural and hospital time [7].

The endoscopic approach is a minimally invasive technique that utilizes small incisions to perform the osteotomies. However, the extent of the osteotomies are constrained by the design and reach of currently available instruments. Conventional instruments used for this approach are rigid and straight tools such as Kerrison punches, rongeurs, Mayo scissors, and elevators [8][9][10][11]. These rigid, non-articulated instruments have limited accessibility with reduced visualization in confined spaces using minimal access incisions [12] that range from 20-40mm in length [9]. As a result, the osteotomies that can be performed are more limited in extent with reduced ability to remodel the cranium. Patients are required to wear a molding helmet to assist with skull remodeling post-operatively for 6-9 months [13], which can be burdensome to patients, or use an internal assistive device such as a spring, which requires a second procedure for removal [14]. Furthermore, certain types of craniosynostosis cannot be effectively treated using an endoscopic approach and thus require open surgery.

Steerable endoscopic tools have been extensively researched and developed for conventional laparoscopic surgeries, including designs based on continuum and serial link structures [15]. Continuum tools are flexible and primarily intended for soft tissue interventions, such as procedures involving the brain, lungs, the endovascular system, gastroenterology [16], and sinuses [17], or for passive conformance within anatomical passageways [18]. In contrast, serial link robotic tools provide relatively higher rigidity [19][20]. Notably, development of motorized bone drilling tools with bending sections have been investigated [19][20]. However, these designs focus on motorized degrees of freedom, resulting in bulky tools that cannot be manually controlled. Moreover, the targeted surgical environments for these tools, such as

bone cyst surgery [19] and femoral osteonecrosis treatment [20, 21], allow the drill to advance freely without the need for surrounding soft tissue protection. Consequently, soft tissue shielding is not a design requirement, and visualization integration is not implemented.

In contrast, craniosynostosis surgery presents a different set of challenges. The skull bone is surrounded by soft tissues, which requires protective shields and an endoscope within the end-effector for safety. This increases the cross-sectional diameter of the tool body. Additionally, the pediatric skull exhibits relatively small bone thickness [22]. These anatomical constraints require the tool to advance such that the bone-cutting tip follows the skull surface closely, while the tool body remains above and unobstructed by the bone.

To solve the above issues, we present a novel bone-cutting tool that is capable of articulating and adapting to the geometry of the skull, providing access to target areas (sutures and cranial bones [23]) through minimal access incisions. The use of this tool would extend the indications and benefits of minimally invasive surgery to patients who currently still require open surgery. Furthermore, the ability to perform more extensive osteotomies may improve the predictability of a minimally invasive approach, eliminating the need for a molding helmet or internal assistive device. This tool would be the first surgical instrument developed specifically for minimally invasive craniotomies (skull bone cuts), and would be a paradigm shift in the surgical treatment of patients with craniosynostosis.

This paper is structured as follows. Technical design goals of the proposed tool will be summarized, followed by the outline of the system design and materials, including the mechanical components and kinematics. The evaluation and corresponding results will then be presented. Finally, the paper will conclude with a discussion of outcomes, limitations, and future works.

## 2 TECHNICAL DESIGN GOALS

Based on the properties and limitations of the existing surgical instruments used during craniosynostosis surgery, the main technical requirements for tool function and performance include dimension, reachability, accuracy, bending stiffness, and bone-cutting ability.

- **Dimensions:** The overall outer diameter of the tool should be less than the combined dimension of conventional tools used in cranial surgery [8], which includes a bone-cutter (4mm), endoscope (4mm), scalp retractor, and suction-irrigation. According to the tools presented in the literature, and used at our in-

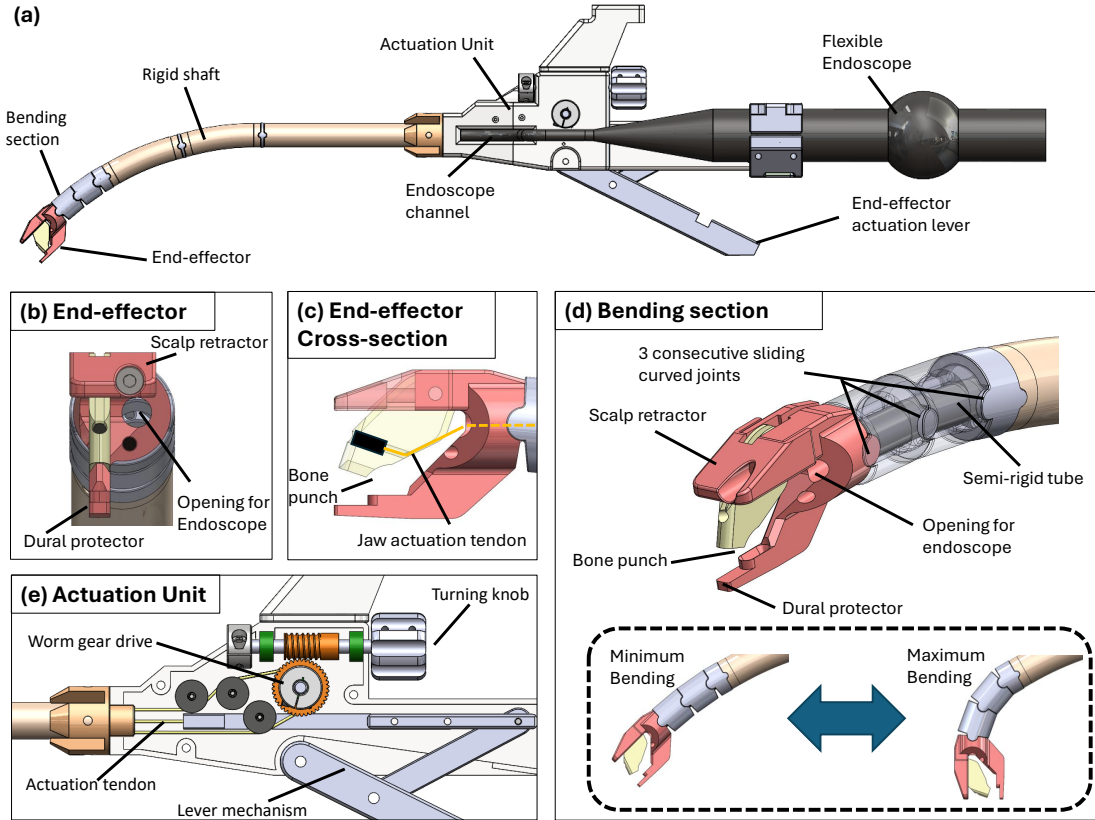


Fig. 1. (a) System overview of the bone-cutting tool including the main components of the device: (b) an end-effector with soft tissue protectors and endoscope channel; (c) a cross-section view of the end-effector illustrating the bone punch mechanism; (d) an articulated bending section with steering capability that consists of three consecutive sliding curved joints and an internal semi-rigid tube; (e) the actuation unit internal components with the tendon-driven mechanism for bending and bone-cutting.

stitution (The Hospital for Sick Children), we determined that the size of the tool diameter should be less than 20mm, which is smaller than the incisions used during minimally invasive craniostomy surgery [9]. In addition, the gap between the bone-cutting jaws should be at least 2mm to effectively grip cranial bone, based on the average pediatric skull thickness [22]. Computed tomography (CT) scan models of 3 craniostomy patients, and data on the circumference of the pediatric skull [22], provides a range for the required radius of curvature of the tool of 30 to 180mm. Thus, the tool must be capable of navigating through paths with varying curvature in this range. In addition, the tool should be lightweight and compact for handheld operation.

- **Reachability coverage:** The reachability of the tool should cover the majority of the skull area using a single vertex incision. The end-effector is required to reach the necessary target areas for craniostomy

surgery with minimal interference from the surrounding soft tissues.

- **Kinematic accuracy:** The mechanism and the kinematic model should ensure the proposed tool is capable of precisely obtaining the desired curvature.
- **Bending stiffness:** The tool should have sufficient bending stiffness to pass through the incision between surrounding tissue, while minimizing unpredictable bending caused by contact with surrounding tissues and enabling stable manipulation.
- **Bone-cutting:** The tool's end-effector should be capable of cutting material with the biomechanical properties of cranial bone at different bending curvatures, with an input force that can be transmitted through a handheld mechanism. The input force should be less than the average grip strength of an adult (493 N for a male and 303 N for a female [24]).

### 3 SYSTEM DESIGN AND MATERIALS

This section presents an overview of the presented instrument, including the mechanical design details, fabrication of each component, and the kinematic design of the system. The design concept is illustrated in Fig 1. The mechanism design comprises an end-effector with a bone-cutting mechanism, a bending section, and an actuation unit with a handle. This system is fully integrated as a standalone device, with the option to attach a flexible endoscope as a modular component.

#### 3.1 End-effector

The end-effector comprises a bone-cutting mechanism, an endoscope channel, a protector for the dura (covering of the brain), and a scalp retractor (see Fig. 1b). The bone-cutting mechanism comprises a bone punch with two jaws: a static lower jaw and a tendon-actuated upper jaw. The closing of the jaws is actuated by a tendon under tension (pulling); however, when the mechanism moves in the opposite direction, the tendon may buckle under compression (pushing). To prevent tendon buckling, a superelastic tube (Nitinol tubing, Chamfr, USA) is used as a guide for the actuation tendon within the hollow shaft. As a result, the tendon and guide tube act as a bowden cable. When the actuation tendon is pushed, the bowden cable system pushes the linkage mechanism to open the jaws, achieving a maximum gap of 4mm. The dural protector shields the brain and dura during bone-cutting and the scalp retractor creates a soft tissue pocket for visualization. The distal end of the flexible tube in the bending section is fixed at the end-effector, creating an opening for an endoscope to visualize the surgical site.

#### 3.2 Bending Section

To overcome the limited reachability of conventional straight tools, we propose an articulated bending section design (see Fig. 1d) and a rigid shaft with a curved section. The bending section is constructed with three consecutive sliding curved joints [25]. This type of joint allows relative movement between two parts along a curved path constrained to a single plane. This type of joint consists of a smaller number of components compared to other types of joints, such as a rolling or hinge joints, as it does not require additional mechanical guiding components such as gears and pins which can be prone to failure. Due to the simplicity of this design, more cross-sectional space can be used for implementation of other functional components, such as a bone-cutting mechanism and visualization channel. Furthermore, a sliding curved joint generally has good resistance to transverse and axial disconnection while maintaining the torsional stiffness nec-

essary to provide forceful actuation such as grasping and cutting. Although sliding curved joints cannot achieve large ranges of motion, three consecutive joints can be used to achieve the required bending to navigate along the curvature of the skull, similar to a continuum mechanism (see Fig. 1c).

In the proposed design, the linkages of the bending section are constructed with rigid metal parts. A semi-rigid polyethylene tube is passed through the joints providing a constant stiffness (see Fig. 1d). A pair of antagonistic tendons are used to actuate the bending section. The tendon pair passes through the bending section and is anchored at the distal end of the linkage mechanism, while the proximal end is fixed to the driving unit. During tendon actuation, the bending curvature changes correspondingly to the change in tendon length, and the bending angle is evenly distributed due to the stiffness of the semi-rigid tube. This tube also acts as a channel for a flexible endoscope to be inserted for visualization, separating a vision channel from an actuation channel. The range of the radius of curvature is constrained by the edge of each linkage, and the multi-link structure is designed to emulate an arc with a radius of curvature between 30 and 180mm. In addition, the current design achieves a diameter of 13.5mm, which is below the incision diameter (20-40mm) and the combined dimensions of the tools currently used during craniostylosis surgery.

#### 3.3 Rigid Shaft

The proximal end of the bending section is connected to a rigid curved shaft. The curved section has a radius of curvature matching the minimum curvature of the skull. The deployment of the proposed tool involves insertion of the device through a small incision. The bone-cutting end-effector is advanced along the skull while performing the osteotomies. As the end-effector proceeds to regions with steeper curvature, the bending section increases its bending angle while the rigid section inserts through the incision following the path of the end-effector.

#### 3.4 Actuation Unit

The actuation unit (See Fig. 1e) is located at the proximal end of the device, which also acts as the handle for manual manipulation. The unit comprises a driving mechanism for the tendons corresponding to bending and bone punching actuation, respectively. For bending, the distal end of the tendons are fixed to the bending section linkages with the proximal end connected to a worm gear mechanism at the driving unit. A worm gear prevents backward driving, allowing maintenance of a joint angle without energy consumption. This non-backdrivability

provides a self-locking feature to the bending section. The worm gear set is made of brass with a reduction ratio of 1:40. A turning knob is connected to the worm gear, allowing the mechanism to be driven manually. The proximal driving unit comprises a linkage mechanism for bone punch actuation. As shown in Fig. 1e, the actuation tendon is routed and anchored to a sliding bar, which is constrained by a linear guide within the handle, allowing only longitudinal movement along the handle axis. By pressing the lever, the linkage mechanism propels the sliding bar proximal, consequently pulling the actuation tendon and closing the punch jaw. When the lever is released, the lever returns to its original position and opens the bone punch. Additionally, a flexible endoscope (11101RP2 Rhino-Laryngo Flexoscope, Karl Storz, Germany) is mounted on the side of the actuation unit and is inserted through the shaft to reach the end-effector. When the full system is deployed for skull bone cutting (Fig. 2b), the field of view of the endoscope encompasses the skull, upper and lower jaws (Fig. 2c).

### 3.5 Prototype Development and Fabrication

A prototype was developed for characterizing tool performance (Fig. 2a). The development of the tool involved computer-aided-design (CAD) using SolidWorks. Components that require high precision and structural integrity, such as the tool shaft, bending section, and gears, were fabricated using computerized numerical control (CNC) machining. The tool shaft is made from 6061 aluminum alloy, the bending section from SUS 316 stainless steel, and the gears from brass. For the actuation mechanism, 1mm diameter stainless steel tendons were utilized. Superelastic nitinol tubes were used for tendon guiding. The device handle, actuation lever, and outer shell were produced using three-dimensional (3D) printing in polylactic acid (PLA) to reduce weight. The prototype, including the endoscope, weighs a total of 700 g. The handle unit has dimensions of  $140 \times 450 \times 58$ mm, making it light and compact for one-handed operation.

### 3.6 Sterilization and Reusability

The instrument is designed to be reusable across multiple procedures. Therefore, material selection was based on compatibility with common sterilization methods for surgical devices. Standard sterilization procedures for Da Vinci surgical instruments involve soaking in a mildly alkaline enzymatic solution, treatment with pressurized cold water, followed by thermal disinfection at  $85^{\circ}\text{C}$ – $93^{\circ}\text{C}$  [26, 27]. Alkaline enzymatic solution and pressurized cold water do not induce reactions in metals and plastics and are therefore compatible with all

materials used in the prototype. The primary components intended for surgical interventions are constructed from 6061 aluminum alloy, SUS 316 stainless steel, and superelastic nitinol, all of which are biocompatible and suitable for high-temperature sterilization [28, 29, 30]. Additionally, since the actuation mechanism components (such as linkages and cables) are made of stainless steel, their performance is not expected to degrade with repeated sterilization cycles and reuse.

Secondly, the handle of the prototype is fabricated using rapid prototyping materials. These materials are not compatible with high-temperature sterilization; however, they can be replaced with sterilization-compatible alternatives during the clinical testing phase. For example, the handle could be fabricated from polypropylene, and internal load-bearing gears and linkages could be replaced with stainless steel [30]. It should be noted that the primary objective of the current prototype is to evaluate the feasibility of the mechanism design. Sterilization and reusability will require further design iteration.

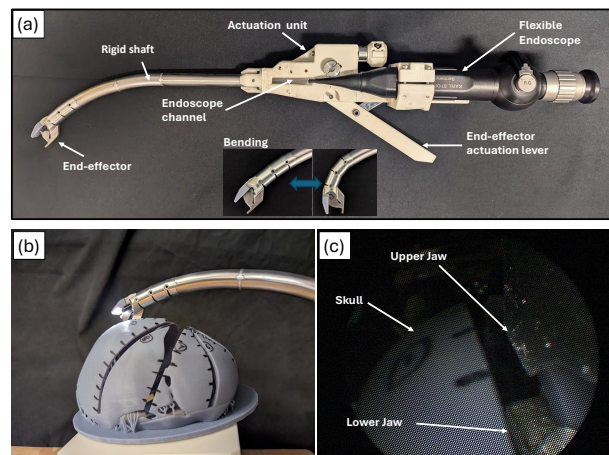


Fig. 2. (a) The prototype of the bone-cutting instrument. (b) Deployment of the prototype using a 3D-printed skull, and (c) visualization from the flexible endoscope tool tip.

### 3.7 Kinematic Relationship and Reachability

In this section, the kinematic framework used to model the articulated bone-cutting instrument is described. The model describes the relationship between the driving input and the pose of the end-effector. Since the instrument operates through a minimal access incision, it is necessary to consider a constraint at the insertion point to represent the scalp. To minimize interference with the

surrounding scalp, translational and rotational motion of the tool at the insertion point should be prevented with insertion of the tool shaft moving tangential to the skull surface through incision. As a result, the motion of the instrument is described with 3 degrees-of-freedom (dof) (yaw, insertion, bending section curvature change).

The kinematic framework involves mapping between the 1) configuration and joint space, 2) the joint and tendon space, as well as 3) the tendon and actuation unit space. This kinematic relationship is used to evaluate the accuracy and the reachability of the tool.

### 3.7.1 Configuration-joint Space Kinematics

The presented tool has one tendon-driven articulated dof, and two manually-manipulated dof at the incision, as described in Fig. 3:

- **Yaw motion:** the motion at the insertion point  $\theta_1$ ;
- **Insertion motion:** the longitudinal movement along the curved shaft where the range of this motion is constrained by the shaft arc length (73.3mm), which is equivalent to rotation around the center of the arc with a corresponding range of  $\theta_2 = [0^\circ, 30^\circ]$ ;
- **Bending section curvature change:** To model the curvature change of a multi-link mechanism, a rigid body model can be used to represent the geometry [25]. This framework can also be used to describe the geometry of a continuum mechanism with constant-curvature by dividing the mechanism into a finite number of segments that are mutually tangent to each other. The bending section of the design is modeled under this kinematic framework by evenly distributing the bending angles with a range of  $\theta_3 = \theta_4 = \theta_5 = [5^\circ, 20^\circ]$ . The length of each link in the mechanism is 13.75mm, and is denoted as  $L_3$ ,  $L_4$ , and  $L_5$ .

The mapping from the joint to configuration space is derived using the Denavit-Hartenberg (DH) parameters [31]. The homogeneous transformation matrix is used to determine the pose of the end-effector  $T_{EE}^0$  with respect to the incision with the transformation:

$$T_{EE}^0 = T_1^0 T_2^1 (T_{\text{bending-section}}) = T_1^0 T_2^1 (T_3^2 T_4^3 T_{EE}^4) \quad (1)$$

$$T = \begin{bmatrix} R(\theta) & P \\ 0 & 1 \end{bmatrix} \in SE(3) \quad (2)$$

where  $T$  is a representation of the  $4 \times 4$  spatial transformation matrix with respect to their axis of rotation.  $R(\theta) \in SO(3)$  and  $P \in \mathbb{R}^3$  represents the orientation and position vector of a frame relative to its parent frame.

### 3.7.2 Joint-tendon Space Kinematics

As illustrated in Fig. 4, the geometric relationship between the rotation angles and tendon displacements of each joint in the bending section can be described using the following:

$$l_d = \frac{1}{2} \sqrt{((L - l_k)^2 + l_T^2)} \quad (3)$$

$$\theta_c = \cos^{-1} \left( 1 - \frac{1}{2} \left( \frac{l_c}{N l_d} \right)^2 \right) \quad (4)$$

$$\theta_{\text{bending}} = \theta_c N \quad (5)$$

where  $L$ ,  $l_k$ ,  $l_T$ , and  $l_d$  are the geometric constants according to the mechanical design:  $L$  is the link length between each joint;  $l_k$  is the length of the guiding within each link;  $l_T$  is the distance between the two tendons;  $l_d$  is the distance between the edge of the tendons guiding and the joint centre. Additionally,  $l_c$  is the tendon displacement;  $\theta_c$  is the bending angle of each joint;  $N$  is the number of joints; and  $\theta_{\text{bending}}$  is the total bending angle of the bending section.

### 3.7.3 Tendon-actuation Unit Space

As shown in Fig. 1e, the bending section is driven by the worm gear mechanism. The reduction ratio of the worm drive used is 1:40. The mapping from the worm gear of the driving unit to tendon space is represented by:

$$l_c = r \theta_{\text{gear}} = \frac{r \theta_{\text{worm}}}{R} \quad (6)$$

where  $\theta_{\text{worm}}$  is the rotation of the worm gear and therefore the input knob;  $\theta_{\text{gear}}$  is the rotation of the gear;  $l_c$  represents the tendon displacements;  $r$  is the radius of the capstan connected to the gear; and  $R$  is the reduction ratio.

## 4 EVALUATION METHODS AND RESULTS

This section presents the evaluation methods and results of the bone-cutting tool testing of its accuracy, bending stiffness, bone-cutting performance, and reachability.

### 4.1 Kinematic Accuracy

The experimental setup for measuring the kinematic accuracy of the prototype, including properties of hysteresis and backlash, is illustrated in Fig. 5. We assessed the orientation of the end-effector by mounting a passive optical navigation marker, which was tracked using an op-

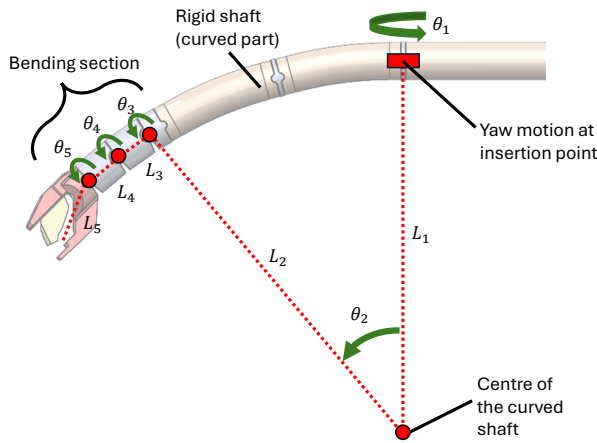


Fig. 3. The kinematic frames describing the motion of the presented instrument: yaw at the insertion point  $\theta_1$ , longitudinal movement along the arc of the shaft  $\theta_2$ , and change in the bending section curvature (even bending angle among the three joints,  $\theta_3 = \theta_4 = \theta_5$ )

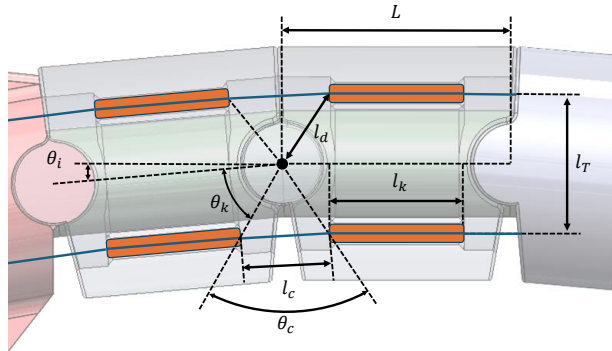


Fig. 4. The geometric relationship between the rotation angles and tendon displacements of each joint of the bending section. The orange parts describe the linear tendons guiding within each linkage.

tical tracker (NDI Polaris Spectra, NDI, Canada). First, the tool tip's orientation was recorded, and the input knob for bending was turned in  $180^\circ$  increments until the tool tip angle reached its physical limit. The input knob was then rotated in the reverse direction until the tool tip returned to its original position. This test was repeated ten times, and the results are shown in Fig. 5b. The blue line represents the actual motion of the tool, while the red line corresponds to the theoretical values based on the kinematic model. The standard deviation of the experimental results are shown as a shaded region around the average values. The arrows indicate the direction of the input. The tool tip reached a maximum angle of  $42.6^\circ$  over 4.75 revolutions, which is  $2.4^\circ$  less than the designed angle ( $45^\circ$  according to the CAD model) and required one additional revolution to reach maximum bending. The maximum observed backlash was 0.5 revolutions at a bending angle of  $0^\circ$ . Whereas at the maximum bending angle, the backlash significantly reduced to 0.25 revolutions.

### 4.2 Stiffness Test

This device is required to have sufficient stiffness to withstand the reaction force generated during interaction with bone. The maximum deflection of the tool tip should not exceed 5mm. This threshold was determined by an experienced craniofacial surgeon at our institution. The cutting force threshold for bone-cutting was experimentally measured to be 5N using a skull saw on a simulated bone plate (PCF40, SawBones, USA) mounted on a force sensor (Mini40, ATI Industrial Automation, USA).

The stiffness of the bending section was evaluated by measuring tool tip deflection under an external load. The experimental setup is shown in Fig. 6a. A measurement weight was attached to the tool tip, applying a downward force, and the displacement was tracked using an optical tracker. The load was then increased to 5N in 1N increments, and the orientation of the end-effector was measured using the same optical tracker setup described in the kinematic test. This was repeated for six bending configurations:  $0^\circ$ ,  $5^\circ$ ,  $20^\circ$ ,  $30^\circ$ ,  $35^\circ$ , and  $40^\circ$ . The results, illustrated in Fig. 6b, indicate that the displacement decreased as the bending angle increased. The deflections remained below 5mm in all cases except for a bending angle of  $0^\circ$ , which deflected the tool tip 5.4mm.

### 4.3 Bone Punch Performance Test

A bone-cutting test was conducted to investigate the ability of the bone punch to cut simulated bone. The experimental setup is shown in Fig 7a. Biomechanical polyurethane foam sheets (PCF 20, 30 and 40, Sawbones, USA) were used to simulate the cranial bone of a cran-

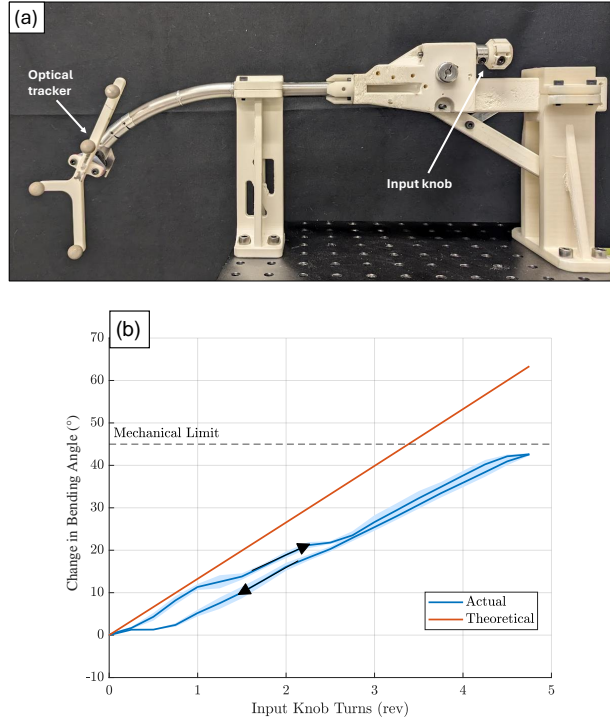


Fig. 5. (a) Experimental setup for kinematic accuracy analysis, (b) Kinematic accuracy results for bending angle change, comparing the measured actual value to the theoretical model.

iosynostosis patient. "PCF" refers to the density unit of pounds per cubic foot. This material has been previously validated for orthopedic device testing [32] in accordance with ASTM International Standard F1839 [33].

Pediatric cranial bone (aged 4 to 10 months) has an approximate thickness of  $2 \pm 0.4$  mm [34]. Based on data from [35], the mechanical properties of piglet calvarium closely resembles that of a human infant, with a reported compressive strength of 2.12 MPa. According to [36], commercial rigid polyurethane foams can simulate this compressive strength with PCF 10 material (ASTM F1839 standards). Furthermore, the mean compressive strength for adult human calvarium is reported to be 15.44 MPa [35], corresponding to PCF 40 material [36]. Therefore, foam sheets of 2.0 mm thickness with three different densities (20, 30, and 40 PCF) were selected to assess bone-cutting performance. This range encompasses a lower bound exceeding the compressive strength of infant cranial bone and an upper bound that overestimates a high-strength condition, providing a broad evaluation spectrum for the bone punch mechanism.

The simulated bone plates were mounted on a fixture. The tool prototype was then mounted and set to a bending range of  $0^\circ - 45^\circ$  in  $15^\circ$  increments. A force gauge (BTE-

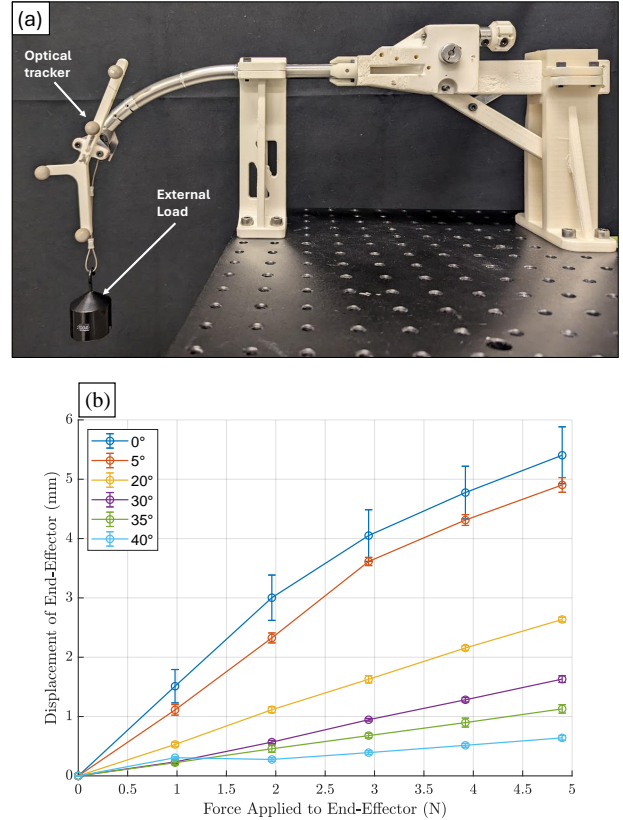


Fig. 6. (a) The experimental setup for the stiffness test. (b) The test results of tool tip displaced from an external force at six bending configurations:  $0^\circ$ ,  $5^\circ$ ,  $20^\circ$ ,  $30^\circ$ ,  $35^\circ$ , and  $40^\circ$ .

500, HFBTE, China) was used to drive the actuation lever at the handle, measuring the force required for a surgeon to perform osteotomies using the tool handle mechanism.

As shown in Fig 7b, the handle force required for full thickness cutting of the 20PCF bone plate ranged from 53.1N to 64.4N as the bending angle increased from  $0^\circ - 45^\circ$ . For the 30PCF bone plate, the force increased to a range of 156.2N to 178.6N. For the 20PCF bone plate, the force varied by 11.3N, while for the 30PCF bone plate, the variation was 22.4N. The prototype was unable to cut the 40PCF bone plate with failure occurring at the stainless steel cable. This 40PCF material represents an overestimation of the mechanical strength (adult skull material) beyond the intended target of this tool, which is designed for pediatric cranial bone applications.

#### 4.4 Reachability Analysis

To ensure maximum reachability of the tool along all areas of the skull, a minimal access incision should be located at the skull vertex (Fig. 8a). Ideally, the instrument

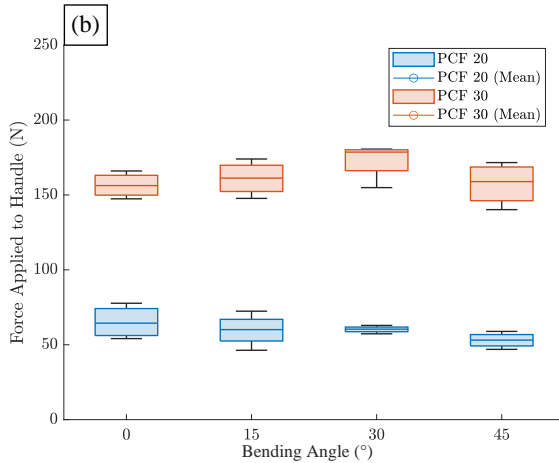
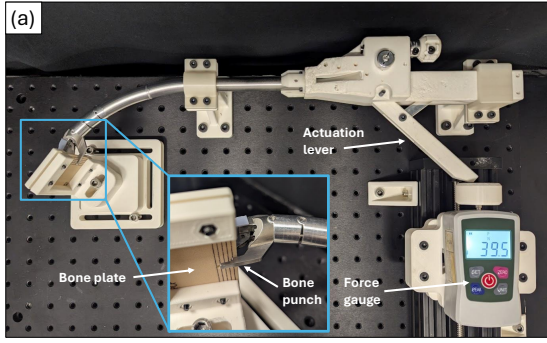


Fig. 7. (a) The experimental setup for the bone punch test, and (b) the result of the force applied to the actuation lever at 4 different bending angles: range from 0°, 15°, 30°, 45°.

shaft should remain at the insertion point and tangential to the surface of the skull to avoid injuring the surrounding soft tissues from excessive retraction. However, due to the flexibility of the scalp, surgeons often stretch the scalp to gain better access.

In this section, two sets of reachability analysis experiments were performed. The first experiment involved setting a fixed constraint that represents the ideal situation where the tool shaft remains at the insertion point and tangential to the skull surface. This constraint ensures that the tool shaft traces the path of the skull without exerting external pressure on the surrounding tissue. A test jig was built to impart this constraint. The second experiment provided a soft constraint, where a silicone scalp was attached to the skull to simulate tool deviation from the insertion that may occur during real surgery from stretching the scalp. In this test, the operator is free to manually move the tool away from the insertion point. The maximum deviation of the tool from the insertion point (mid-shaft to skull surface distance) was measured.

Table 1. Cutting paths and their corresponding locations

Path	Location
1	Sagittal suture
2	Parietal bone (left)
3	Coronal suture (left)
4	Frontal bone (left)
5	Metopic suture
6	Frontal bone (right)
7	Coronal suture (right)
8	Parietal bone (right)

For the two experiments, eight osteotomy paths (Table 1) along the skull surface were created to represent the overall tool reachability. Each path starts from the vertex and ends at the distal extent of the skull inferiorly. These paths cover locations along the cranial sutures (sagittal, metopic, coronal) as well as cranial bone areas that may require osteotomies between the sutures (see Fig. 8b).

Both experiments were repeated three times on three common types of craniosynostosis: sagittal (path 1), metopic (path 5), and unicoronal (path 3). The skull models used in this section were 3D-printed using a Photon M3 Max (Anycubic, Hong Kong) based on CT scan models of craniosynostosis patients to simulate skull bone geometry.

#### 4.4.1 Hard Constraint

The reachability in the first experiment was defined as the area that the tool tip can reach on the skull surface. The experimental setup is illustrated in Fig. 8a. During the test, the bone-cutting tool was mounted on the constraint jig. The operator adjusts the bending angle such that the tool tip remains on the surface of the skull as the tool advances along the path. The motion of the tool tip was tracked using the optical tracker. When the tool tip deviates from the skull and can no longer follow the surface, the deviation point is recorded, and the area beyond this point is defined as "out of reach."

The reachability results are shown in Fig. 8c-8e, where the blue area represents the edge of each target cutting path on the skull that is defined as the full extent of the osteotomy target. The orange area represents the experimental results of the tools reach. For the three craniosynostosis cases, the prototype was able to cover 72.2%, 71.1%, and 78.4% of the target area for the sagittal, metopic, and unicoronal skulls, respectively.

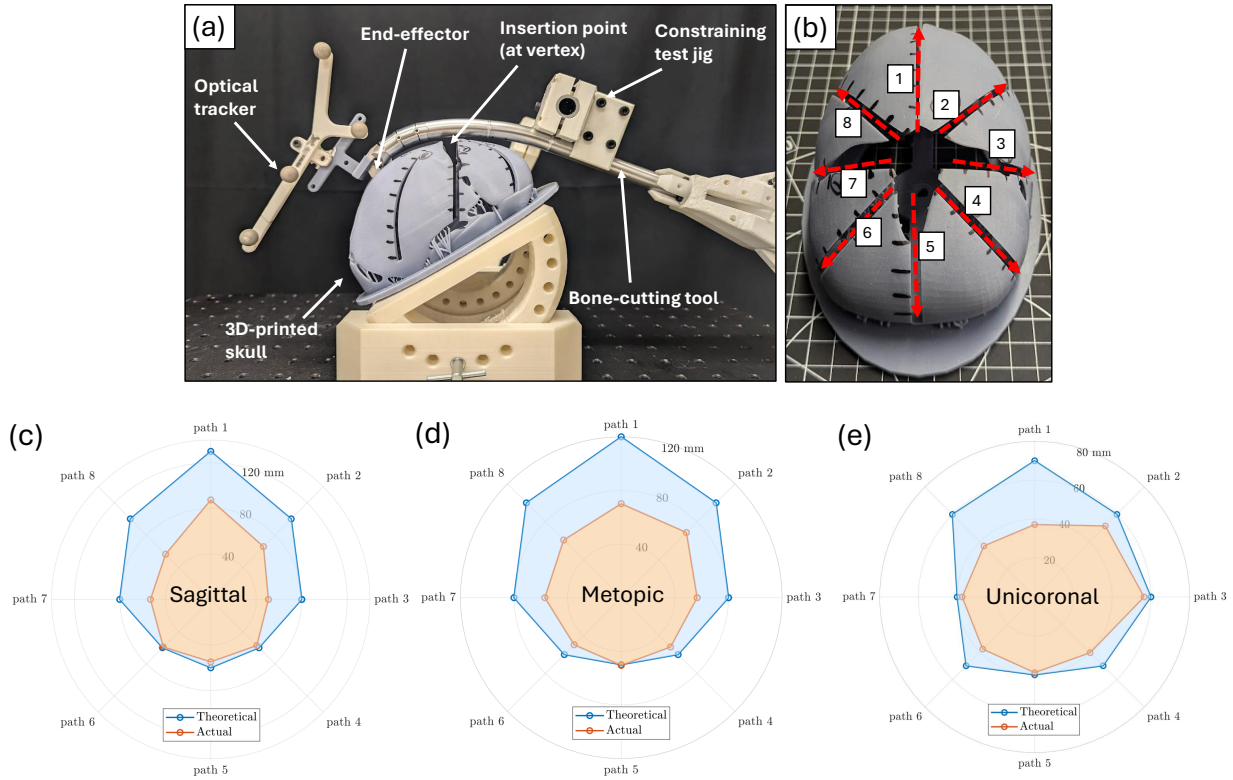


Fig. 8. (a) Reachability experimental setup with a hard constraint at the insertion point. (b) Eight paths on the skull for the tool to trace. The results of the reachability experiment for each craniosynostosis skull type tested: (c) sagittal, (d) metopic, (e) unicornal. The blue area represents the total skull path area. The orange area represents the reachability results of the tool.

#### 4.4.2 Soft Constraint

In the second experiment, a piece of silicone sheet was secured to the sagittal craniosynostosis skull to simulate the soft constraint of the scalp during surgery. A 20mm vertex incision was made on the simulated scalp. The tool was then inserted through the incision and advanced to the most distal point along each of the eight paths. During each path test, the flexible scalp was allowed to stretch to pivot the tool at the insertion to reach the most distal point along each path. The vertical distance between the vertex and the mid-point of the tool shaft was measured, indicating the deviation of the tool and the insertion point.

As illustrated in Fig 9, when the tool reaches the distal point, the operator is required to lift the scalp off the skull. For the eight paths, the deviation was less than 11mm for all cases, ranging from 1.23-10.88mm. These values represent feasible scalp stretch (qualitatively assessed by a craniofacial surgeon at our institution).

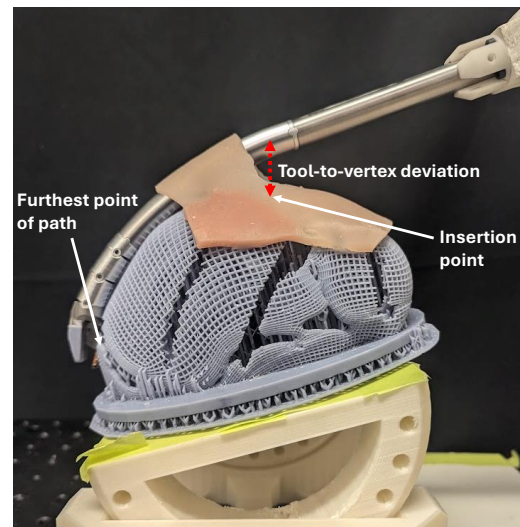


Fig. 9. The experimental setup for the reachability experiment where the tool shift deviates at the skull vertex. This is required to reach the most distal point along each path. The example here shows path 1 on a sagittal craniosynostosis skull.

## 5 DISCUSSION AND CONCLUSION

The tool presented introduces a novel approach to cranosynostosis surgery. The instrument enhances reachability along the skull using minimal access incisions while maintaining key functional requirements regarding dimensions, end-effector accuracy, stiffness, and bone-cutting capability. These technical specifications are essential for broadening the scope of minimally invasive cranosynostosis surgical procedures. The instrument is designed to perform bone-cutting within confined spaces through minimal access incisions, addressing a significant limitation of existing tools.

The kinematic testing demonstrated some inaccuracies between the kinematic model and actual mechanism. This can be attributed to mechanical backlash and tendon stretch in the transmission mechanism. However, a major objective of this research is to present the concept of the first minimally invasive bone cutting tool. The inaccuracies can be compensated by using visual feedback. Since bending actuation is user-controlled based on the endoscopic view, the operator can manually increase the number of input knob revolutions until the tool reaches the desired target. The maximum observed backlash was 0.5 revolutions and required one additional revolution to reach maximum bending. While the actual motion differs from the theoretical kinematics, the results are consistent and repeatable. As a result, the experimental data can serve as a reliable mapping between the input and the bending angle. This mapping can be used for future developments that involves robotic assistance. Nevertheless, future work is required to improve the accuracy of the tools motion. This can be achieved by using higher elastic modulus materials for the tendons, improving fabrication processing, reducing mechanical backlash, and implementing a position feedback.

The stiffness test demonstrated the effectiveness of the tendon-driven bending section using sliding joints with an integrated flexible tube. The end-effector demonstrated small displacements with external forces up to 5N (Fig. 6). This indicated that the tool can maintain a target position during forceful application during bone cutting.

The instrument also demonstrated the effectiveness of the bone-cutting mechanism using simulated bone (20-40PCF). The bone punch is capable of cutting materials with biomechanical properties and thickness similar to infant cranial bone across different bending configurations. The force required to use the handle lever mechanism is lower than the average adult grip strength and can be operated comfortably by a surgeon. Although the required grip force slightly increased with larger bending angles (at maximum 22.4N), this variation is lower than the average adult grip strength [24], and users are unlikely to

perceive a disproportionate increase in effort as the configuration changes. However, the current bone punch was unable to cut the 40PCF bone plate due to cable failure, representing the upper limit of the current design. It is important to note that the 20 and 30PCF bone plates already have compressive strength values higher than pediatric cranial bone, whereas the 40PCF material corresponds to the strength of an adult human skull. In conclusion, the current prototype provides sufficient cutting strength for the intended application of pediatric cranial bone but is not suitable for adult cranial surgeries. Future work should consider utilizing cables with higher failure strength to further enhance the tools ability to cut tougher and thicker material for broader range of applications.

The reachability results demonstrated the tools ability to reach the majority of the skull area for three types of cranosynostosis skulls tested without deviation from the skull surface. The tool was able to cover 72.2%, 71.1%, and 78.4% of the target area for the sagittal, metopic, and unicoronal skulls. The remaining areas can be reached by shifting the tool shaft from the insertion point, causing a feasible amount of scalp stretch of less than 11mm. To completely eliminate this deviation, additional degrees of freedom would be needed to adjust the tool's shape to better conform to the skull's curvature. Conventional minimally invasive surgical (MIS) tools have limited reach and hence more limited cutting techniques can be performed. Currently available MIS technique includes endoscopic strip [37], and extended strip craniectomy [38]. With the new tool, more extensive cutting patterns would be possible, potentially allowing the surgeon to use techniques that previously can only be performed during open surgery, such as barrel-stave osteotomies [39]. As shown in [7], these extensive cutting techniques negate the need for assistive devices such as a helmet or internal springs.

Future research will focus on refining the tool's design, fabrication, and functionalities. Key objectives include enhancing osteotomy speed through powered bone-cutting mechanisms and improving maneuverability by incorporating additional degrees of freedom at the end-effector. During osteotomy procedures, bone chips may accumulate at the punch tip, requiring periodic retraction for debris removal, similar to conventional bone punches. The current end-effector mechanical design protects the hinges and actuation cables from debris. As a result, no jamming was observed during any of the tests conducted in this study. Future iterations will incorporate suction-irrigation features to eliminate the need for retraction during surgery. Further studies will also evaluate the stiffness and deformation of the continuum bending section under high external loads to minimize kinematic control errors. Future study will also assess the ergonomics and usability

ity of the tool by performing a surgeon usability study involving qualitative questionnaires provided to multiple surgeons who test the tool. Animal and human cadaver experiments will then be conducted to further evaluate the clinical feasibility. Sterilization of the tool is also an important consideration that will be addressed as we progress towards clinical studies using the tool. As the tool comprises no electrical components, we believe that this will be addressed by redesign to include sterilization safe materials.

In conclusion, a novel articulating bone-cutting tool was developed that demonstrates high reachability using an articulated bending section. The tool represents an evolution in craniostyostosis surgery that may provide the benefits of minimally invasive surgery to more patients with craniostyostosis.

#### ACKNOWLEDGEMENTS

This research was supported by Natural Sciences and Engineering Research Council, Canada Graduate Scholarship-Doctoral (NSERC CGS-D) and Canadian Institutes of Health Research (CIHR).

#### REFERENCES

- [1] Flaherty, K., Singh, N., and Richtsmeier, J. T., 2016, "Understanding craniostyostosis as a growth disorder," *WIREs Developmental Biology*, **5**, 7, pp. 429–459.
- [2] Shlobin, N. A., Baticulon, R. E., Ortega, C. A., Du, L., Bonfield, C. M., Wray, A., Forrest, C. R., and Dewan, M. C., 2022, "Global epidemiology of craniostyostosis: A systematic review and meta-analysis," *World Neurosurgery*, **164**, 8, pp. 413–423.e3.
- [3] Speltz, M. L., Collett, B. R., Wallace, E. R., Starr, J. R., Craddock, M. M., Buono, L., Cunningham, M., and Kapp-Simon, K., 2015, "Intellectual and academic functioning of school-age children with single-suture craniostyostosis," *Pediatrics*, **135**, 3, pp. e615–e623.
- [4] Kilipiris, E., Horn, F., and Poruban, D., 2019, "Open cranial vault reconstruction in the surgical correction of craniostyostosis. a review of 100 cases," *International Journal of Oral and Maxillofacial Surgery*, **48**, 5, p. 140.
- [5] Zakhary, G. M., Montes, D. M., Woerner, J. E., Nottarianni, C., and Ghali, G., 2014, "Surgical correction of craniostyostosis. a review of 100 cases," *Journal of Cranio-Maxillofacial Surgery*, **42**, 12, pp. 1684–1691.
- [6] Goyal, A., Lu, V. M., Yolcu, Y. U., Elminawy, M., and Daniels, D. J., 2018, "Endoscopic versus open approach in craniostyostosis repair: a systematic review and meta-analysis of perioperative outcomes," *Child's Nervous System*, **34**, 9, pp. 1627–1637.
- [7] Shah, M. N., Kane, A. A., Petersen, J. D., Woo, A. S., Naidoo, S. D., and Smyth, M. D., 2011, "Endoscopically assisted versus open repair of sagittal craniostyostosis: the st. louis children's hospital experience," *Journal of Neurosurgery: Pediatrics*, **8**, 8, pp. 165–170.
- [8] Jimenez, D. F., and Moon, H. S., 2022, "Endoscopic approaches to craniostyostosis," *Atlas of the Oral and Maxillofacial Surgery Clinics*, **30**, 3, pp. 63–73.
- [9] Jimenez, D. F., and Barone, C. M., 2010, "Endoscopic techniques for craniostyostosis," *Atlas of the Oral and Maxillofacial Surgery Clinics*, **18**, 9, pp. 93–107.
- [10] Barone, C. M., and Jimenez, D. F., 2004, "Endoscopic approach to coronal craniostyostosis," *Clinics in Plastic Surgery*, **31**, 7, pp. 415–422.
- [11] Jeelani, Y., and Proctor, M. R., 2021, "Endoscopic surgical treatment of bilateral coronal craniostyostosis," *Neurosurgical Focus: Video*, **4**, 4, p. V13.
- [12] Han, R. H., Nguyen, D. C., Bruck, B. S., Skolnick, G. B., Yarbrough, C. K., Naidoo, S. D., Patel, K. B., Kane, A. A., Woo, A. S., and Smyth, M. D., 2016, "Characterization of complications associated with open and endoscopic craniostyostosis surgery at a single institution," *Journal of Neurosurgery: Pediatrics*, **17**, 3, pp. 361–370.
- [13] Rottgers, S. A., Lohani, S., and Proctor, M. R., 2016, "Outcomes of endoscopic suturectomy with postoperative helmet therapy in bilateral coronal craniostyostosis," *Journal of Neurosurgery: Pediatrics*, **18**, 9, pp. 281–286.
- [14] Governale, L. S., and Ching, J. A., 2021, "Spring-assisted minimally invasive repair of sagittal craniostyostosis," *Neurosurgical Focus: Video*, **4**, 4, p. V8.
- [15] Burgner-Kahrs, J., Rucker, D. C., and Choset, H., 2015, "Continuum robots for medical applications: A survey," *IEEE Transactions on Robotics*, **31**, 12, pp. 1261–1280.
- [16] da Veiga, T., Chandler, J. H., Lloyd, P., Pittiglio, G., Wilkinson, N. J., Hoshier, A. K., Harris, R. A., and Valdastrì, P., 2020, "Challenges of continuum robots in clinical context: a review," *Progress in Biomedical Engineering*, **2**, 8, p. 032003.
- [17] Wang, X., Yan, J., Ma, X., Chan, J. Y. K., Taylor, R. H., Cheng, S. S., and Au, K. W. S., 2022, "Hybrid-structure hand-held robotic endo-

- scope for sinus surgery with enhanced distal dexterity,” *IEEE/ASME Transactions on Mechatronics*, **27**, 8, pp. 1863–1872.
- [18] Dupont, P. E., Simaan, N., Choset, H., and Rucker, C., 2022, “Continuum robots for medical interventions,” *Proceedings of the IEEE*, **110**, 7, pp. 847–870.
- [19] Solzbacher, R. M., Kim, S., Lee, S., Kim, H., Joung, S., Lee, H.-J., and Hong, J., 2022, “Bone cyst surgery robot with bendable drilling and remote control,” *Journal of Computational Design and Engineering*, **9**, 11, pp. 2495–2505.
- [20] Wang, Y., Zheng, H., Taylor, R. H., and Au, K. W. S., 2022, “A handheld steerable surgical drill with a novel miniaturized articulated joint module for dexterous confined-space bone work,” *IEEE Transactions on Biomedical Engineering*, **69**, 9, pp. 2926–2934.
- [21] Alambeigi, F., Wang, Y., Sefati, S., Gao, C., Murphy, R. J., Iordachita, I., Taylor, R. H., Khanuja, H., and Armand, M., 2017, “A curved-drilling approach in core decompression of the femoral head osteonecrosis using a continuum manipulator,” *IEEE Robotics and Automation Letters*, **2**, 7, pp. 1480–1487.
- [22] Li, Z., Park, B.-K., Liu, W., Zhang, J., Reed, M. P., Rupp, J. D., Hoff, C. N., and Hu, J., 2015, “A statistical skull geometry model for children 0-3 years old,” *PLOS ONE*, **10**, 5, p. e0127322.
- [23] Turgut, M., Tubbs, R. S., Turgut, A. T., and Dumont, A. S., eds., 2021, *The Sutures of the Skull* Springer International Publishing.
- [24] Pratt, J., Vito, G. D., Narici, M., Segurado, R., Dolan, J., Conroy, J., and Boreham, C., 2021, “Grip strength performance from 9431 participants of the genofit study: normative data and associated factors,” *GeroScience*, **43**, 10, pp. 2533–2546.
- [25] Jelínek, F., Arkenbout, E. A., Henselmans, P. W. J., Pessers, R., and Breedveld, P., 2015, “Classification of joints used in steerable instruments for minimally invasive surgery—a review of the state of the art,” *Journal of Medical Devices*, **9**, 3.
- [26] Intuitive, 2018, da vinci xi instrument reprocessing instructions.
- [27] Harrington, R. E., Guda, T., Lambert, B., and Martin, J., 2020, *Sterilization and Disinfection of Biomaterials for Medical Devices* Elsevier.
- [28] Thierry, B., Tabrizian, M., Savadogo, O., and Yahia, L., 2000, “Effects of sterilization processes on niti alloy: Surface characterization,” *Journal of Biomedical Materials Research*, **49**, 1, pp. 88–98.
- [29] Kumar, P., Talele, S., Deshpande, S., Ghyar, R., Rout, S., and Ravi, B., 2023, “Design, analysis and experimental validation of a novel 7-degrees of freedom instrument for laparoscopic surgeries,” *Annals of Biomedical Engineering*, **51**, 4, pp. 751–770.
- [30] Protolabs, 2022, Common autoclave compatible materials, 10.
- [31] Khalil, W., and Kleinfinger, J., 1986, “A new geometric notation for open and closed-loop robots,” In Proceedings. 1986 IEEE International Conference on Robotics and Automation, IEEE, pp. 1174–1179.
- [32] Sawbones, 2023, Biomechanical test materials validation studies, 2.
- [33] , 2021, Specification for rigid polyurethane foam for use as a standard material for testing orthopaedic devices and instruments, 2.
- [34] Igo, B. J., Cottler, P. S., Black, J. S., and Panzer, M. B., 2021, “The mechanical and microstructural properties of the pediatric skull,” *Journal of the Mechanical Behavior of Biomedical Materials*, **120**, 8, p. 104578.
- [35] Li, Z., Hu, J., Reed, M. P., Rupp, J. D., Hoff, C. N., Zhang, J., and Cheng, B., 2011, “Development, validation, and application of a parametric pediatric head finite element model for impact simulations,” *Annals of Biomedical Engineering*, **39**, 12, pp. 2984–2997.
- [36] Calvert, K. L., Trumble, K. P., Webster, T. J., and Kirkpatrick, L. A., 2010, “Characterization of commercial rigid polyurethane foams used as bone analogs for implant testing,” *Journal of Materials Science: Materials in Medicine*, **21**, 5, pp. 1453–1461.
- [37] Garland, C. B., Camison, L., Dong, S. M., Mai, R. S., Losee, J. E., and Goldstein, J. A., 2018, “Variability in minimally invasive surgery for sagittal craniosynostosis,” *Journal of Craniofacial Surgery*, **29**, 1, pp. 14–20.
- [38] Adamo, M. A., and Pollack, I. F., 2010, “A single-center experience with symptomatic postoperative calvarial growth restriction after extended strip craniectomy for sagittal craniosynostosis,” *Journal of Neurosurgery: Pediatrics*, **5**, 1, pp. 131–135.
- [39] Jimenez, D. F., Barone, C. M., McGee, M. E., Cartwright, C. C., and Baker, C. L., 2004, “Endoscopy-assisted wide-vertex craniectomy, barrel stave osteotomies, and postoperative helmet molding therapy in the management of sagittal suture craniosynostosis,” *Journal of Neurosurgery: Pediatrics*, **100**, 5, pp. 407–417.